

## Article

# Highly Porous Layered Double Hydroxide and Mixed Metal Oxide by Sacrificial Bio-Template, Egg White Foam

Vidya Chandrabose <sup>1</sup>, Ji won Park <sup>1,2</sup>, Sang Yong Jung <sup>1,3</sup> , Kang Kyun Wang <sup>4,\*</sup> and Jae-Min Oh <sup>1,\*</sup> 

<sup>1</sup> Department of Energy and Materials Engineering, Dongguk University, Seoul 04620, Republic of Korea; cbvidya1997@gmail.com (V.C.); qkrwldnjs324@naver.com (J.w.P.); syjung05@naver.com (S.Y.J.)

<sup>2</sup> Developing Product Quality Innovation Team, LG Display, Paju 10845, Republic of Korea

<sup>3</sup> SN Bioscience, 422-Na, LH Business Growth Center, 54 Changeop-ro, Sujeong-gu, Seongnam-si 13449, Republic of Korea

<sup>4</sup> BI Bio-Photonics Co., Ltd., Gimpo-si 10090, Republic of Korea

\* Correspondence: biprimelab2020@gmail.com (K.K.W.); jaemin.oh@dongguk.edu (J.-M.O.)

**Abstract:** Highly porous layered double hydroxide (LDH) and its calcined mixed metal oxide (MMO) were obtained by utilizing egg white (EW) as a biogenic porous template. The LDH was prepared through coprecipitation under the existence of a beaten EW meringue, and the corresponding MMO was obtained by calcining LDH at 500 °C. According to X-ray diffraction, the crystal structure of LDH and MMO was well-developed with or without EW. In contrast, the crystallinity analyses and microscopic investigations clearly showed differences in the particle orientation in the presence of EW; the protein arrangement in the EW foam induced the ordered orientation of LDH platelets along proteins, resulting in well-developed inter-particle pores. As a result, the distinctive particle arrangement in EW-templated samples compared with non-templated ones showed dramatically enhanced specific surface area and porosity. The nitrogen adsorption–desorption isotherm exhibited that the high specific surface area was attributed to the homogeneous nanopores in EW-templated LDH and MMO, which originated from the sacrificial role of the EW.

**Keywords:** mixed metal oxides; layered double hydroxides; egg white foam; biogenic template; porous structure



**Citation:** Chandrabose, V.; Park, J.w.; Jung, S.Y.; Wang, K.K.; Oh, J.-M. Highly Porous Layered Double Hydroxide and Mixed Metal Oxide by Sacrificial Bio-Template, Egg White Foam. *Crystals* **2023**, *13*, 1603. <https://doi.org/10.3390/cryst13111603>

Academic Editors: Leticia Santamaria, Miguel A. Vicente and Antonio Gil Bravo

Received: 9 October 2023

Revised: 29 October 2023

Accepted: 13 November 2023

Published: 20 November 2023



**Copyright:** © 2023 by the authors. Licensee MDPI, Basel, Switzerland. This article is an open access article distributed under the terms and conditions of the Creative Commons Attribution (CC BY) license (<https://creativecommons.org/licenses/by/4.0/>).

## 1. Introduction

Highly porous mixed metal oxide (MMO) ceramics have attracted wide attention due to their various compositions, huge specific surface areas, large pore volume, controllable physicochemical properties, and high stability. These MMOs are generally obtained through the solid-state phase transformation upon the calcination process by applying the appropriate temperature to the precursors. After thermal treatment, the resulting MMOs generally possess superior properties than the precursors [1–4]. These MMOs are exploited in various applications as catalysts, adsorbents, sensors, drug carriers, and so on [5–11]. As most of the above-mentioned applications utilized the surface interaction between MMO and target species, researchers developed synthetic approaches to induce high surface area with controlled porosity such as the soft template, hard template, and self-templated methods [12,13].

Layered double hydroxide (LDH), which is known as anionic clay, consists of positively charged mixed metal hydroxide layers that are separated by interlayer anions and water molecules. The LDH structure is formed with  $M(OH)_6$  octahedral units sharing edges to build brucite-like  $M(OH)_2$  layers. These octahedral sites consist of both divalent and trivalent metal cations. The chemical formula of LDH is generally expressed as  $[M(II)_{1-x}M(III)_x(OH)_2]^{x+}A^{n-}_{x/n}$ , in which the  $x$  approximately ranges from 0.2 to 0.4 [14]. Upon thermal treatment, LDH undergoes dehydration of the water molecules on the surface as well as in the interlayer region, dehydroxylation, and the loss of anions in the

interlayer, resulting in the evolution of MMO. According to the previous literature, the lamellar structure of LDH partially collapses during calcination, and a partial trivalent ion migrates from the octahedral site to the tetrahedral site, together with the evolution of the periclase phase (MgO). The calcination process is an efficient way of synthesizing MMO due to the homogeneous metal arrangement, as the pristine LDH tends to have an ordered orientation of its divalent and trivalent cations. This homogeneous distribution of the trivalent ion assures the even action of certain metal species, possibly the trivalent one, as an adsorption or catalytic site. Moreover, the pore structure evolution upon calcination enhances the specific surface area [15–19].

Previous studies indicated that the porous nature of materials is the most important property to determine the efficiency of toxic species removal, especially in water contaminants [20–22]. Furthermore, porosity in the electrical material could enhance the catalytic and electrical activity. Electrocatalysts for hydrogen evolution and oxygen evolution reactions could achieve high performance due to the porous structure and high surface area [23,24]. Template-assisted synthesis is a widely utilized method to generate regular porosity in metal oxides [25,26]. A representative advantage of templated synthesis is the easy tuning of the final products according to the nature of the template [27,28]. There were reports of combining the calcination of LDH and the templated method to obtain homogeneous MMO with high porosity [29,30]. For instance, ordered mesoporous NiAl-MMO was prepared, using pluronic-F127 as a template, by the soft template method with NiAl-LDH as a precursor [31]. Our group previously synthesized mesoporous MgAl-MMO with homogenous pores, by using P-123 as a template [32].

Although the above-mentioned methods resulted in homogeneous MMO with a high specific surface area thanks to the LDH precursor and ordered templates, the process has limitations when applied on an industrial scale due to the potential environmental issue and the lower economical accessibility of surfactants and templating polymers. In order to address this issue and find a green process, we focused on the utility of the biogenic template method. The sacrificial template method is an efficient way to more precisely control the pore size for the synthesis of porous LDH or MMO. There were several works on the synthesis of LDH utilizing bio-templates. An et al. prepared MgAl-LDH utilizing casein and caprolactam as a core material to be coated by LDH layers [33]. Their approach was successful in obtaining flame-retardant LDH; however, it was not related to the porous structure. The ZnAl-LDH was synthesized on the surface of a legume in order to take advantage of the biomorphic morphology [34]. In contrast, Sobhana et al. synthesized LDH networks based on cellulose to obtain a high specific surface area [35]. Considering the research, it is fairly feasible that LDH could be prepared with a hierarchical pore structure utilizing various bio-template candidates. In the current study, we expand the concept to naturally borne biomaterials such as egg white (EW), which is used for the synthesis of ordered nanoparticles. EW is rich in amino acids and proteins [36], which play stabilizing and controlling roles in metal oxide formation [37]. Metal oxide nanoparticles such as iron oxide [38], titanium dioxide [39,40], and cerium oxides [41] could be synthesized in a homogeneous size under the presence of an EW bio-template. EW mainly consists of proteins having either a globular or filament shape [42,43]. Upon agitation, the combination of proteins produces a foam through the incorporation of air bubbles. The protein moieties are rapidly self-assembled around the air bubble to create a macromolecular network, leading to the coagulation; thus, EW acts as a self-aggregated template for porous metal oxide (first step of Figure 1a). We recently reported that porous MMO could be synthesized utilizing albumin as a bio-template through the repetitive calcination–reconstruction process [44]; however, the development of porosity had limitations when a single albumin is utilized as a template. In order to obtain a systematic molecular arrangement of a biogenic template, it is suggested to take advantage of natural protein components in EW. The as-synthesized porous EWH and EWO can act as promising candidates for the adsorption and removal of pollutants and catalysis, as a biocompatible host, owing to their hierarchical pores and a high specific surface area.

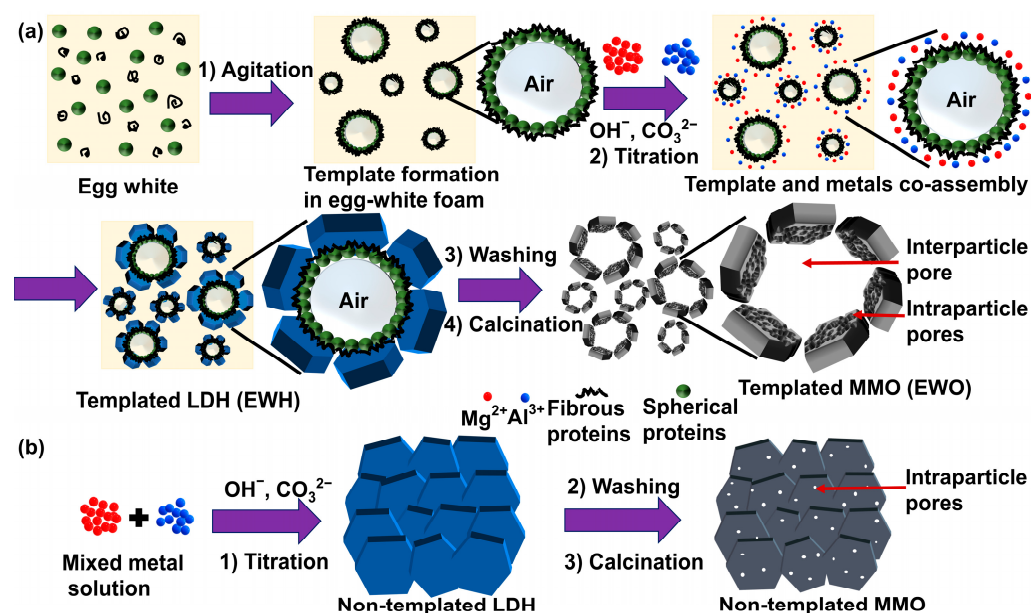


**Figure 1.** Schematic illustration of (a) EW-templated LDH (EWH) and (b) non-templated LDH.

Herein, we suggest synthetic procedures for LDH and MMO with high porosity and specific surface area utilizing EW foam as a biogenic template, as illustrated in Figure 1. The egg-white-templated LDH was synthesized using the conventional coprecipitation method. The egg white proteins undergo unwinding and are surrounded by the air pockets after the agitation. The rapidly self-assembled proteins around the air pockets form a macromolecular network in the egg white foam, which acts as the sacrificial porogenic template for the synthesis. The conjoint self-assembly between the metal precursors and EW proteins results in a hierarchical architecture and facilitates the formation of the homogenous nanoporous structure by directly growing LDH on or around the proteins. As the proteins in EW foam develop large networks, we hypothesized that the protein moiety does not inhibit the crystal growth of LDH; rather, the protein network could act as the template to order the LDH particles. In other words, the air pockets covered by the protein arrays would remain as pores by arranging LDH particles around them. In this manner, the assembly of LDH layers would lose its preferred particle orientation along the crystallographic *c*-axis and obtain a large particle–particle space through the assembly of particles. Both EW-templated and non-templated LDH were prepared in this study, and their properties were compared in terms of crystal structure, textural morphology, and porosity, to elucidate the role of EW as a bio-template in the synthesis of LDH and MMO.

## 2. Materials and Methods

### 2.1. Materials

Magnesium nitrate hexahydrate ( $\text{Mg}(\text{NO}_3)_2 \cdot 6\text{H}_2\text{O}$ ) and aluminum nitrate nonahydrate ( $\text{Al}(\text{NO}_3)_3 \cdot 9\text{H}_2\text{O}$ ), were purchased from Sigma-Aldrich, Inc., St. Louis, MO, USA. Sodium hydroxide ( $\text{NaOH}$ ) and sodium bicarbonate ( $\text{NaHCO}_3$ ) were obtained from Daejung Chemicals & Metal Co., Ltd., Seoul, Republic of Korea. Eggs were purchased from a local market in Seoul, South Korea. All the reagents and material used without further purification.

### 2.2. Synthesis of Egg-White-Templated LDH (EWH) and Corresponding Mixed Metal Oxide (EWO)

The egg-white-templated LDH was synthesized following the conventional coprecipitation method [45]. First, EW foam was prepared by whipping the egg white with a household mechanical blender for 5 min in a glass beaker to make foam. Approximately 3.13 g of egg white foam was taken in a 3-neck round bottom flask and subjected to the templated synthesis of LDH. The metal solution and alkaline solution were prepared, and

both solutions were located in dropping funnels, which are connected to two necks of the flask. The metal solution was prepared by dissolving 1.53 g of  $\text{Mg}(\text{NO}_3)_2 \cdot 6\text{H}_2\text{O}$  (0.03 mol) and 1.12 g of  $\text{Al}(\text{NO}_3)_3 \cdot 9\text{H}_2\text{O}$  (0.015 mol) in 200 mL deionized water. The alkaline solution was made by dissolving 1.63 g NaOH (0.227 mol) and 2.54 g of  $\text{NaHCO}_3$  (0.168 mol) in 180 mL of deionized water. Both metal solution and alkaline solution were simultaneously added to the flask, which already contained egg white foam, under stirring. The adding rate of the metal solution and alkaline solution was carefully maintained to adjust the pH of the reaction system constant at  $\sim 9.5$ . The reaction mixture was processed for 24 h under room temperature, and the obtained suspension was centrifuged at 8000 rpm for 4 min to collect EWH precipitate. The product was washed with deionized water three times in order to remove unreacted ion and salt; finally, the EWH powder was collected by lyophilization. The mixed metal oxide originated from EWH (EWO) was obtained by calcination of EWH at 500 °C for 3 h. Typically, the EWH powder ( $\sim 1$  g) was located in an alumina boat and placed in a muffle furnace without any lid on the boat. The temperature was raised up to 500 °C at 0.8 °C/min of heating rate. After a designated time of 3 h, the sample was cooled down under ambient condition. Finally, the powder, EWO, was collected and stored under dried condition.

### 2.3. Synthesis of LDH and MMO without EW

In order to investigate the role of the EW template in the structure and porosity, both LDH and MMO without the EW were prepared for comparison. For the synthesis of LDH, mixed metal solution and an alkaline solution were similarly prepared as described in Section 2.2. Then, the synthesis of the LDH was carried out via the conventional coprecipitation method, in which alkaline solution and metal solution were simultaneously dropped in to the round bottom flask at pH  $\sim 9.5$ . After 24 h of aging at room temperature, the precipitate was collected by centrifugation, washed with deionized water three times, and lyophilized to obtain LDH. The MMO from the LDH was obtained by calcining LDH at 500 °C for 3 h with a 0.8 °C/min heating rate in a muffle furnace.

### 2.4. Characterization

The crystal structure of the four samples was elucidated by powder X-ray diffraction (XRD, Ultima IV, Rigaku, Tokyo, Japan) using Cu  $K\alpha$  radiation ( $\lambda = 1.5405 \text{ \AA}$ ) at 50 kV and 40 mA. The powder diffraction patterns were collected in the range of  $2\theta$  from 5 to 80°, with an interval of 0.02° and a scan speed of 0.5°/min. The crystallite size of the samples was calculated by using Scherrer's equation, as shown below [46].

$$\tau = (0.9\lambda)/(B \cos \theta)$$

where  $\tau$  = crystallite size ( $\text{\AA}$ ),  $\lambda$  = X-ray wavelength (1.5405  $\text{\AA}$ ),  $B$  = full-width at half-maximum (FWHM), and  $\theta$  = Bragg's angle.

The particle size and surface morphology of the particles were analyzed by scanning electron microscopy (SEM, JEOL-7100F, Tokyo, Japan) at an acceleration voltage of 15 kV. The powdered sample was gently spread on the carbon tape, and loosely bound powder was blown away with an air blower. The specimen was coated with Pt/Pd by vacuum sputtering for 1 min. Detailed particle size and morphology along with lattice structure patterns were investigated by a high-resolution transmission electron microscope (HR-TEM, G2 ChemiSTEM Cs probe, FEI Company, Hillsboro, MA, USA) at an accelerating voltage of 200 kV. After the sample was dispersed in ethanol, the suspension was dropped on the Cu 200 mesh grid. Then, the specimen was dried in the oven at 60 °C. The  $\text{N}_2$  adsorption–desorption isotherms were determined by BEL-SORP-mini II (Microtrac BEL, Inc., Tokyo, Japan) at 77 K. After the samples were degassed at 313 K in vacuum condition overnight. The specific surface area, mean pore diameter, and mean pore volume were calculated through Brunauer–Emmett–Teller (BET) theory. The pore size distribution was calculated through Barrett–Joyner–Halenda (BJH) model.

### 3. Results and Discussion

#### 3.1. X-ray Diffraction Patterns

The crystal structure of LDHs and MMOs were analyzed by powder X-ray diffraction. The diffractograms of EWH and LDH showed typical patterns of hydrotalcite ( $\text{Mg}_3\text{Al}(\text{OH})_8(\text{CO}_3)_{0.5}\text{-LDH}$ ; JCPDS no. 22-0700), exhibiting distinctive peaks at a  $2\theta$  value of  $11.58^\circ$ ,  $23.16^\circ$ ,  $34.75^\circ$ ,  $39.16^\circ$ ,  $46.20^\circ$ ,  $60.83^\circ$ , and  $62.06^\circ$  attributed to the (003), (006), (012), (015), (018), (110), and (113) crystal planes, respectively (Figure 2a,b) [47]. The XRD patterns of both templated and non-templated LDH indicate that both were synthesized without any significant impurity, regardless of the template method. The same lattice parameter values of both EWH and LDH ( $a = 3.04 \text{ \AA}$ ,  $c = 22.9 \text{ \AA}$ ) suggested that EW protein moieties neither prevented LDH crystals from growing nor incorporated them into the interlayer space of the LDH framework. The FT-IR spectrum of all the samples is given in Figure S1 (see in Supplementary Materials). The IR spectra of all samples showed a broad peak at  $3430 \text{ cm}^{-1}$  due to the O-H stretching vibration of the water molecules. The peak that appeared at  $1646 \text{ cm}^{-1}$  for all materials was attributed to the bending vibration of O-H groups. The peak appearing at  $1385 \text{ cm}^{-1}$  was assigned to the interlayer  $\text{CO}_3^{2-}$  anions. The peak obtained between  $500$  and  $800 \text{ cm}^{-1}$  corresponds to the metal–oxygen bonds in the LDH framework [48]. It is considered that the protein moieties present in the egg white foam could be homogeneously adsorbed on the LDH surface rather than being introduced in between the interlayers of the metal hydroxide due to the large size of the proteins. Both calcined products, EWO and MMO, were determined to have a periclase phase ( $\text{MgO}$ ; JCPDS no. 45-0946), showing representative (200) and (220) peaks at  $43.3^\circ$  and  $62.7^\circ$ , respectively (Figure 2c,d) [49], suggesting that the formation of metal oxide phase is irrespective of the EW template. Generally, Mg-Al LDH upon calcination underwent dehydration, dehydroxylation, and decarbonization leading to the phase transformation from the LDH phase to their corresponding mixed metal oxide form. It is well-known that the calcination of the metal double hydroxide at a moderate temperature of  $400\text{--}600^\circ\text{C}$  results in the evolution of divalent metal oxide, MMO, with a periclase ( $\text{MgO}$ ) phase. During the calcination process, most of the divalent cations maintained their corresponding coordination site in the octahedral center, whereas the trivalent cations underwent partial migration from the octahedral site to the tetrahedral site. In this manner, the major building block of both templated and non-templated MMOs consists of  $\text{MgO}$  rather than  $\text{Al}_2\text{O}_3$  [50].

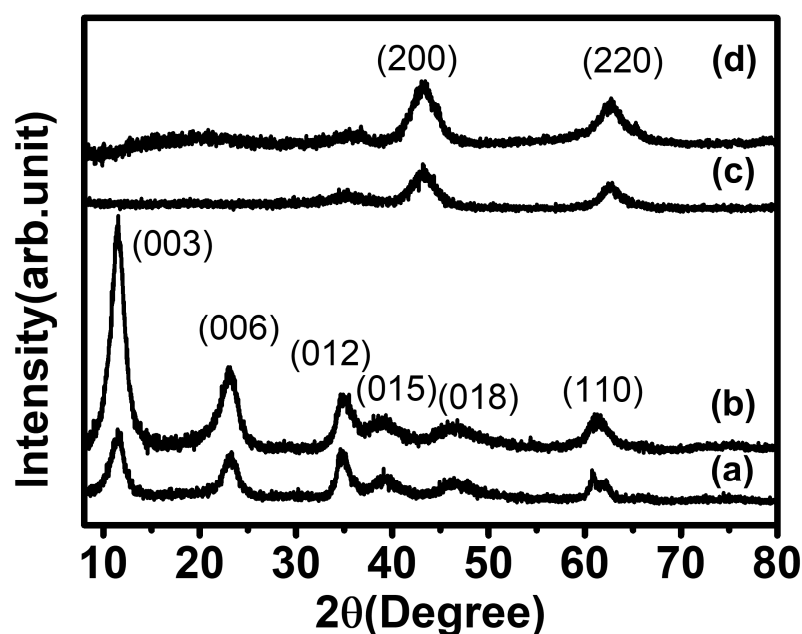
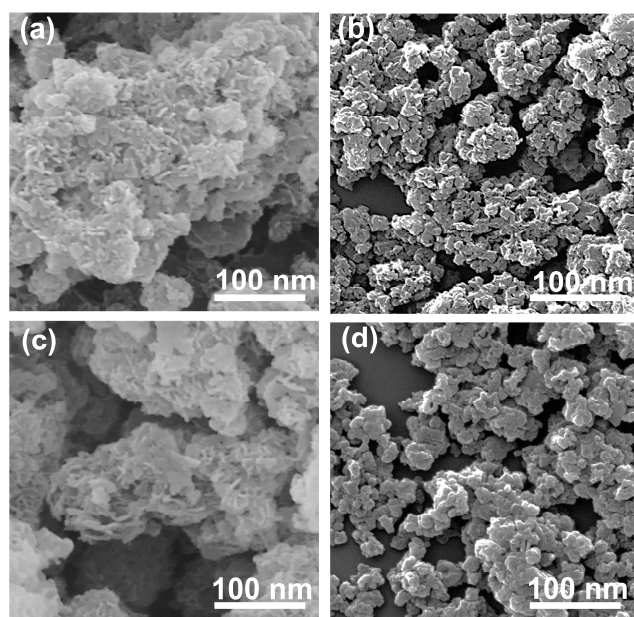


Figure 2. X-ray diffraction patterns of (a) EWH, (b) pristine LDH, (c) EWO, and (d) MMO.

It is worth noting here that the peak intensity of EWH was different from that of LDH. The diffractogram of LDH showed strong (001) diffraction compared with other lattice peaks, while the (001) peaks of EWH were fairly comparable to those of the lattice peaks. In detail, the peak area ratio of (003)/(110) was 0.17 and 6.22 for EWH and LDH, respectively, exhibiting the predominant c-axis array in LDH rather than in EWH. As LDH is a layered material, the particles tend to orient in a two-dimensional way, increasing the (001) signal much higher than the (hkl) components [51]. However, EW-templated LDH (EWH) had a fairly comparable ratio. We hypothesized that the LDH particles prepared with EW grew along the protein moiety covering the air pocket, and, thus, the preferred orientation along the c-axis was avoided. Interestingly, the peak intensity ratio in both EWO and MMO was fairly comparable; the peak area ratio (200)/(220) was 1.27 and 1.41, respectively, for MMO and EWO. It was attributed to the small crystallites formed by the calcination of LDH, as in the previous report, showing a similar crystallite size of MMO regardless of the orientation of the starting LDH particles [52]. The calculated crystallite size using Scherrer's equation is provided in Table S1 (see in Supplementary Materials). We could not observe any significant changes in the lattice parameters or the crystallite size in the crystalline structure of MgO from either templated or non-templated LDH. Therefore, it was concluded that the crystalline structure of the EW-templated and non-templated LDH and MMO was almost the same and that the crystal formation process was not seriously affected by the EW template.

### 3.2. Scanning Electron Microscopy

The morphology and arrangement of particles were investigated through scanning electron microscopy. The SEM images showed that the morphology of the EWH and EWO were fairly similar showing typical sand rose shapes (Figure 3a,c) [53]. The sand rose structure of the EWH and EWO can be attributed to the edge-to-face interaction among the LDH plate-like particles. The orientation of plate-like particles in both EWH and EWO suggested particle growth along the protein moiety in EW foam. The existence of protein in the EW foam not only hindered the particle agglomeration of LDH but also arranged the particles with proper interparticle space. In contrast, the SEM images of both LDH and MMO exhibited large lumps and were densely assembled, being hundreds of nanometers in size (Figure 3b,d). The particle size and morphology of the non-templated MMO were comparable with that of the pristine LDH formed by the conventional method, as shown in Figure 3b,d according to the previous report [54]. The non-templated LDH and its MMO show few interparticle pores due to the aggregation of LDH particles. It is generally known that LDH particles tend to get together through strong interparticle interaction. Although the particle sizes of the LDHs and MMOs were not precisely determined, both LDHs seemed to have comparable particle dimensions, of approximately 75 nm for the lateral size. Therefore, the different crystallinity between EWH and LDH observed in the XRD (Figure 2) was attributed to the different particle orientations, not to the crystallite size. The SEM images of the templated and non-templated MMOs also suggested that the particle morphologies of their corresponding pristine LDH are almost preserved after thermal treatment. As a result, the lattice structures of the EWH and LDH did not undergo a collapse of the metal hydroxide layers after dehydration.



**Figure 3.** SEM images of (a) EWH, (b) LDH, (c) EWO, and (d) MMO.

### 3.3. Transmission Electron Microscopy

The morphological difference as well as the interparticle structure of the samples were evaluated in detail by TEM. According to the TEM images of EWH and EWO (Figure 4a,c), the particles were arranged in various directions, possibly along the protein moiety in the EW foam. The morphology of both EWH and EWO showed randomly oriented and crumpled lamellar sheets with thin layers, as observed in the SEM images. According to Figure 1, as the agitation of EW incorporates air bubbles, the protein moieties started to align around the bubbles. The rearranged protein molecules resulted in the formation of a network, for which strength is obtained by the mixing of both spherical and globular proteins. The addition of an alkalizing agent formed amorphous clusters of  $Mg_xAl_y(OH)_z$  around the protein network. Upon the aging process, the amorphous clusters gathered to form a metal double hydroxide network around the porous skeleton of EW. The interaction between the metal cations and negatively charged protein moieties is thought to facilitate the seed formation of  $Mg_xAl_y(OH)_z$  clusters. Compared with Figure 4a, more interparticle space is evident in Figure 4c, which confirmed that the porous architecture of the EWO sample displays high porosity. This was confirmed by the random orientation of the egg-white-templated LDH and MMO resulting in distinctive interparticle pores. Pores were more obvious in EWO (Figure 4c) than in EWH (Figure 4a), as the thermal decomposition process clearly removed the egg white template and air pocket to produce interparticle pores. EWH and EWO apparently exhibited interparticle spaces, which lead to a higher specific surface area than non-templated LDH. This is because the air pockets with the protein networks surrounding EWH particles leave a cavity during the thermal process. Furthermore, EWO would have intraparticle pores, which can be formed from the metal oxide domains that evolve upon calcination and can be linked by the  $Al^{3+}$  that migrates to the tetrahedral site. In other words, the local disorder that occurred during the thermal treatment leads to the collapse of the metal hydroxide layers and forms O-Al-O bonds, resulting in the evolution of intraparticle mesopores. In contrast, LDH and MMO showed an agglomeration of particles (Figure 4b,d). Due to the particle aggregation in pristine LDH, the interparticle pore was not prominent when compared with EWH. The specific surface area of non-templated LDH and MMO would be lower than the templated one due to the fewer interparticles present due to the particle's aggregation. The degree of orientation in MMO particles was more ordered, as we suggested in Figure 1, resulting in the reduction of the porosity in MMO. In conclusion, the evolution of the interparticle pores drastically enhances the removal amount through multi-layer adsorption, and the intraparticle pores

would act as adsorption sites for small molecules. EW-templated LDH and MMO would increase activity and selectivity for adsorbates.

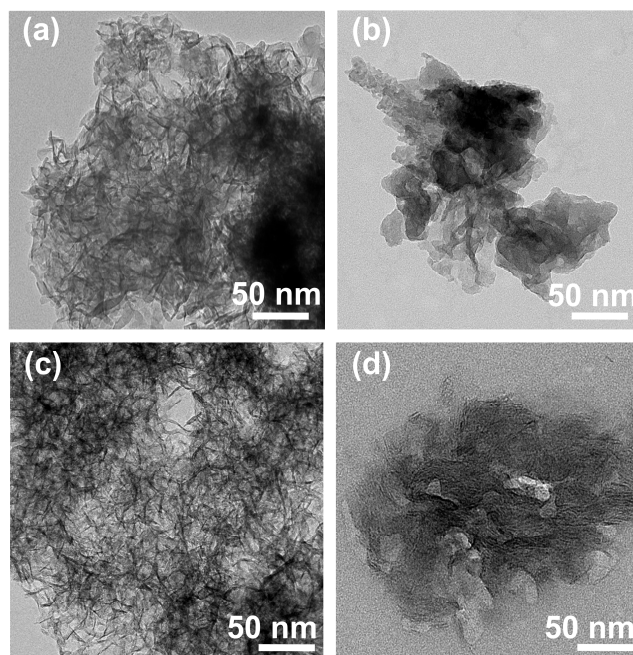


**Figure 4.** TEM images of (a) EWH, (b) LDH, (c) EWO, and (d) MMO.

The orientation of the particles was also analyzed by a high-magnification image. The lattice fringe images of EWH and EWO are illustrated in Figure 5a,b, in which a set of white lines depicts the lattice fringes. The set of white lines indicated the random orientation of the particles toward the different directions. As shown in Figure 5a,b, both EWH and EWO revealed lattice fringes corresponding to the planes of (015) and (018) and (200) and (220), respectively. As a result, ring patterns can be observed in the fast Fourier transform (FFT) image of both EWH and EWO. The solid circular lines in Figure 5c,d attributed to the plane of (018) and (015) and (200) and (220) were observed in FFT patterns in both EWH and EWO, confirming the random arrangement of crystallites.

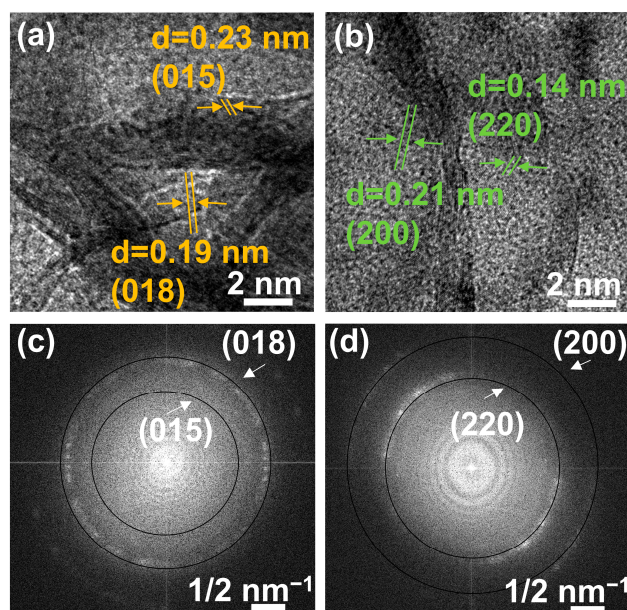


**Figure 5.** Lattice fringe images of (a) EWH, (b) EWO, and FFT patterns of (c) EWH and (d) EWO.

### 3.4. N<sub>2</sub> Adsorption–Desorption Isotherms

The N<sub>2</sub> adsorption–desorption isotherms were measured in order to confirm the difference in porosity of materials coming from the EW template. The untemplated samples, LDH and MMO, showed type III adsorption according to the International Union of Pure and Applied Chemistry (IUPAC) classification (Figure 6a), suggesting a nonporous nature [55]. LDH is generally considered nonporous with lower adsorbent–adsorbate interaction, and they only provide particle surface as an adsorption site [56]. When LDH was calcined at moderate temperature, an increase in the specific surface area and an evolution of some pores through degassing, dehydration, and dehydroxylation usually occurred. However, in the current sample, we could only observe a slight increase in  $S_{\text{BET}}$  (Table 1), without a significant change in N<sub>2</sub> adsorption behavior. This was attributed to the ordered c-axis orientation–particle agglomeration of the LDH particles whose arrangement was preserved even after calcination. The evolution of the intraparticle pore accounted for the pore's increase in the enhancement of  $S_{\text{BET}}$ ; however, a notable porous structure was not found in MMO.

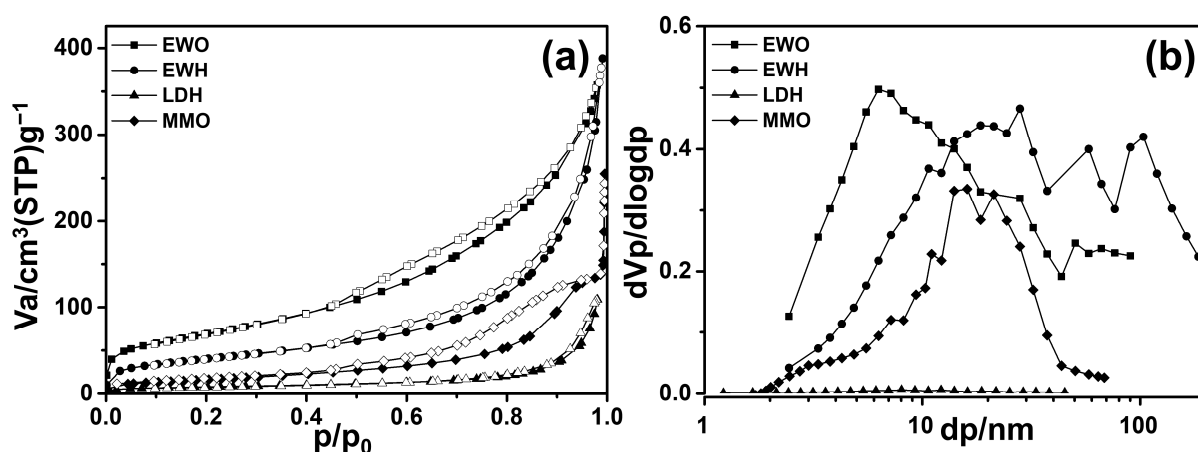


**Figure 6.** (a) N<sub>2</sub> adsorption and desorption isotherms (closed symbol—adsorption, open symbol—desorption) and (b) BJH pore size distribution plots for EWO, EWH, LDH, and MMO.

**Table 1.** Porosity information of EWH, EWO, LDH, and MMO.

Parameters	LDH	MMO	EWH	EWO
$S_{\text{BET}}$ (m <sup>2</sup> /g)	29	62	144	248
Pore volume (cm <sup>3</sup> /g)	0.2	0.2	0.6	0.6
Mean pore diameter (nm)	24	14	16	9

Different from the non-templated samples, both EWH and EWO exhibited type II adsorption, implying that there is facilitated adsorption in well-developed pore structures (Figure 6b). As summarized in Table 1, the  $S_{\text{BET}}$  value of EWH and EWO was much higher than that of their non-templated counterparts. This would be strongly related to the preferred crystal growth in LDH along the EW protein (Figure 1). The progenic sacrificial template was believed to be concentrated around the LDH crystal due to the surface adsorption of the protein moieties (both globular and fibrous proteins). The EWH crystals appeared to develop around the self-aggregated sacrificial template. In addition to the stabilizing ability of the proteins in egg white foam, the arrangement of EW proteins could result in the evolution of appropriate pores. The two calcined samples, EWO and MMO, exhibited hysteresis, which can be assigned to either H3 or H4 and indicates the evolution of the intraparticle pore. (Figure 6a) [57]. This hysteresis could be interpreted as plate-like or slit-like pores, and the porous structures arose from the partial collapse of the hydroxide layer through the dehydroxylation of the metal hydroxide framework. Although both metal oxides evolved slit-like pores, the efficiency of pore development was

higher in EWO, as their particle arrangement was like a house-of-cards structure coming from the particle arrangement along the protein moiety [58].

The quantitative analyses on surface area and pore volume were encouraging, as we could confirm the template role of EW. The  $S_{\text{BET}}$  value of EWH was as high as  $145 \text{ m}^2/\text{g}$ , which was by far larger than that of the non-templated LDH in this study ( $29 \text{ m}^2/\text{g}$ ) and in other studies in the literature ( $\sim 50 \text{ m}^2/\text{g}$  and  $9 \text{ m}^2/\text{g}$ ) for Mg-Al-LDH [34,59]. After the calcination of EWH, the surface area was enhanced to  $248 \text{ m}^2/\text{g}$  due to the complicated processes—the thermal decomposition of EW proteins preserving the interparticle arrangement as well as the evolution of the intraparticle pore. The specific surface area of the templated MMO was higher than the MMOs obtained from the LDHs in previous studies which was  $\sim 135 \text{ m}^2 \text{ g}^{-1}$  synthesized through the hydrothermal reaction for both Mg-Al, Mg-Ga and the bio-templated method for Zn-Al MMO respectively [34,60]. In addition, the pore size distribution was evaluated with BJH plot distribution to confirm the pore structure (Figure 6b). It was observed that after calcination the pore size tended to more narrowly distribute due to the evolution of interparticle or intraparticle pores. The pore volume of EWO ( $0.6 \text{ cm}^3/\text{g}$ ) was more than twice that of MMO ( $0.2 \text{ m}^3/\text{g}$ ), showing the sacrificial role of EW in the development of pores during calcination. This is because the egg white proteins were homogeneously incorporated between the LDH particles, which upon calcination evolve into homogeneously distributed pores in the LDH framework. The mean pore diameter of EWO was 9 nm, which was much smaller than that of MMO (14 nm), which confirms that homogeneous mesopores could be obtained by the action of the EW template. The values in Table 1 were obtained by BET calculation, and the error range was less than 3% [61]. Taking into account this information, the  $S_{\text{BET}}$  as well as the pore volume difference between templated and non-templated is statistically meaningful. Therefore, the pore analyses clearly showed that EW foam played a crucial role in the formation of interparticle pores.

#### 4. Conclusions

We successfully synthesized highly porous EWO with a controllable pore size via the green method by using EW foam as the bio-template. The particle ordering of EWH was preserved after calcination, developing both interparticle and intraparticle pores. The  $S_{\text{BET}}$  value of EWH was found to be  $144 \text{ m}^2/\text{g}$ , which was larger than that of non-templated LDH ( $29 \text{ m}^2/\text{g}$ ). Highly porous EWO was obtained with a high BET surface area of  $248 \text{ m}^2/\text{g}$ , with the aid of the egg white template. The outcome of using a natural egg white template resulted in enhanced porosity and specific surface area. The present study reveals that egg white foam can act as a porous skeleton during the template synthesis. This bio-template method can be utilized for producing well-defined porosity in materials such as ceramics and inorganic materials with enhanced surface area and narrow size pore distribution. Taking into account the high specific surface area and large pore volume of EW-templated LDH as well as the intrinsic anion affinity of LDH, the current materials could be utilized for water treatment to remove various aqueous pollutants such as toxic organic dyes.

**Supplementary Materials:** The following supporting information can be downloaded at: <https://www.mdpi.com/article/10.3390/cryst13111603/s1>, Figure S1: FT-IR spectra of (a) EWH, (b) LDH, (c) EWO, and (d) MMO; Table S1: The crystallite size of EWH, LDH, EWO, and MMO.

**Author Contributions:** Conceptualization V.C., J.-M.O. and K.K.W.; methodology, J.w.P. and S.Y.J.; software, V.C.; validation, J.w.P. and S.Y.J.; formal analysis, V.C.; investigation, V.C., J.w.P. and S.Y.J.; resources, J.w.P. and S.Y.J.; data curation, V.C.; writing—original draft preparation, V.C.; writing—review and editing, J.-M.O. and K.K.W.; visualization, V.C.; supervision, J.-M.O. and K.K.W.; project administration, J.-M.O. and K.K.W.; funding acquisition, J.-M.O. and K.K.W. All authors have read and agreed to the published version of the manuscript.

**Funding:** This work was financially supported by the Korea Water Cluster (KWC) as the Korea Water Cluster Project Lab and the National Research Foundation of Korea (NRF), funded by the Korean government (MSIT) (no. RS-2023-00242687) and was partially funded by the Korea Institute of Planning and Evaluation for Technology in Food, Agriculture and Forestry (IPET) through the

High Value-Added Food Technology Development Program, funded by the Ministry of Agriculture, Food and Rural Affairs (MAFRA) (321043-05) and the results in this study was based on the “Leaders in Industry-university Cooperation 3.0” Project, supported by the Ministry of Education and National Research Foundation of Korea.

**Data Availability Statement:** All data generated or analyzed during this study are included in this article.

**Conflicts of Interest:** Author Ji won Park was employed by the company Developing Product Quality Innovation Team, LG Display; Sang Yong Jung was employed by the company SN Bioscience, LH Business Growth Center; Kang Kyun Wang was employed by the company BI Bio-Photonics Co., Ltd. The remaining authors declare that the research was conducted in the absence of any commercial or financial relationships that could be construed as a potential conflict of interest.

## References

1. Zhao, X.; Zhang, F.; Xu, S.; Evans, D.G.; Duan, X. From Layered Double Hydroxides to ZnO-Based Mixed Metal Oxides by Thermal Decomposition: Transformation Mechanism and UV-Blocking Properties of the Product. *Chem. Mater.* **2010**, *22*, 3933–3942. [[CrossRef](#)]
2. Liu, S.; Liu, J.; Wang, T.; Wang, C.; Ge, Z.; Liu, J.; Hao, X.; Du, N.; Xiao, H. Preparation and Photovoltaic Properties of Dye-Sensitized Solar Cells Based on Zinc Titanium Mixed Metal Oxides. *Colloids Surf. A* **2019**, *568*, 59–65. [[CrossRef](#)]
3. Takemoto, M.; Tokudome, Y.; Murata, H.; Okada, K.; Takahashi, M.; Nakahira, A. Synthesis of High-Specific-Surface-Area Li-Al Mixed Metal Oxide: Through Nanoseed-Assisted Growth of Layered Double Hydroxide. *Appl. Clay Sci.* **2021**, *203*, 106006. [[CrossRef](#)]
4. Abderrazek, K.; Najoua, F.S.; Srasra, E. Synthesis and Characterization of [Zn-Al] LDH: Study of the Effect of Calcination on the Photocatalytic Activity. *Appl. Clay Sci.* **2016**, *119*, 229–235. [[CrossRef](#)]
5. Dou, Y.; Han, J.; Wang, T.; Wei, M.; Evans, D.G.; Duan, X. Fabrication of MMO–TiO<sub>2</sub> One-Dimensional Photonic Crystal and Its Application as a Colorimetric Sensor. *J. Mater. Chem.* **2012**, *22*, 14001–14007. [[CrossRef](#)]
6. Seisenbaeva, G.A.; Moloney, M.P.; Tekoriute, R.; Hardy-Dessources, A.; Nedelec, J.M.; Gun’ko, Y.K.; Kessler, V.G. Biomimetic Synthesis of Hierarchically Porous Nanostructured Metal Oxide Microparticles-Potential Scaffolds for Drug Delivery and Catalysis. *Langmuir* **2010**, *26*, 9809–9817. [[CrossRef](#)]
7. Ko, S.J.; Yamaguchi, T.; Salles, F.; Oh, J.M. Systematic Utilization of Layered Double Hydroxide Nanosheets for Effective Removal of Methyl Orange from an Aqueous System by  $\pi$ - $\pi$  Stacking-Induced Nanoconfinement. *J. Environ. Manag.* **2021**, *277*, 111455. [[CrossRef](#)]
8. Choy, J.H.; Choi, S.J.; Oh, J.M.; Park, T. Clay Minerals and Layered Double Hydroxides for Novel Biological Applications. *Appl. Clay Sci.* **2007**, *36*, 122–132. [[CrossRef](#)]
9. Mishra, G.; Dash, B.; Pandey, S. Layered Double Hydroxides: A Brief Review from Fundamentals to Application as Evolving Biomaterials. *Appl. Clay Sci.* **2018**, *153*, 172–186. [[CrossRef](#)]
10. Li, E.; Xu, Z.P.; Rudolph, V. MgCoAl-LDH Derived Heterogeneous Catalysts for the Ethanol Transesterification of Canola Oil to Biodiesel. *Appl. Catal. B Environ.* **2009**, *88*, 42–49. [[CrossRef](#)]
11. Védrine, J. Heterogeneous Catalysis on Metal Oxides. *Catalysts* **2017**, *7*, 341. [[CrossRef](#)]
12. Kaplin, I.Y.; Lokteva, E.S.; Golubina, E.V.; Lunin, V.V. Template Synthesis of Porous Ceria-Based Catalysts for Environmental Application. *Molecules* **2020**, *25*, 4242. [[CrossRef](#)]
13. Ying, J.Y.; Mehnert, C.P.; Wong, M.S. Synthesis and Applications of Supramolecular-Templated Mesoporous Materials. *Angew. Chem. Int. Ed.* **1999**, *38*, 56–77. [[CrossRef](#)]
14. Lee, S.-B.; Ko, E.-H.; Park, J.Y.; Oh, J.-M. Mixed Metal Oxide by Calcination of Layered Double Hydroxide: Parameters Affecting Specific Surface Area. *Nanomaterials* **2021**, *11*, 1153. [[CrossRef](#)]
15. Li, Y.-J.; Qi, T.-T.; Dong, Y.-N.; Hou, W.-H.; Chu, G.-W.; Zhang, L.-L.; Sun, B.-C. Synthesized Ni/MMO Catalysts via Ultrathin Ni-Al-LDH in a Rotating Packed Bed for Hydrogenation of Maleic Anhydride. *Fuel* **2022**, *326*, 125035. [[CrossRef](#)]
16. Ram Reddy, M.K.; Xu, Z.P.; Lu, G.Q.; Da Costa, J.C.D. Layered Double Hydroxides for CO<sub>2</sub> Capture: Structure Evolution and Regeneration. *Ind. Eng. Chem. Res.* **2006**, *45*, 7504–7509. [[CrossRef](#)]
17. Veerabhadrapa, M.G.; Maroto-Valer, M.M.; Chen, Y.; Garcia, S. Layered Double Hydroxides-Based Mixed Metal Oxides: Development of Novel Structured Sorbents for CO<sub>2</sub> Capture Applications. *ACS Appl. Mater. Interfaces* **2021**, *13*, 11805–11813. [[CrossRef](#)]
18. Zhang, L.; Liu, J.; Xiao, H.; Liu, D.; Qin, Y.; Wu, H.; Li, H.; Du, N.; Hou, W. Preparation and Properties of Mixed Metal Oxides Based Layered Double Hydroxide as Anode Materials for Dye-Sensitized Solar Cell. *Chem. Eng. J.* **2014**, *250*, 1–5. [[CrossRef](#)]
19. Chandrabose, V.; Kim, T.; Park, J.W.; Jung, S.-Y.; Oh, J.-M. Effect of Tetrahedrally Coordinated Al on the Surface Acidity of Mg-Al Binary Mixed Oxides. *Molecules* **2023**, *28*, 6072. [[CrossRef](#)]
20. Almanassra, I.W.; Chatla, A.; Zakaria, Y.; Kochkodan, V.; Shanableh, A.; Laoui, T.; Atieh, M.A. Palm Leaves Based Biochar: Advanced Material Characterization and Heavy Metal Adsorption Study. *Biomass Convers. Biorefinery* **2022**, 1–20. [[CrossRef](#)]

21. Khalil, A.K.A.; Dweiri, F.; Almanassra, I.W.; Chatla, A.; Atieh, M.A. Mg-Al Layered Double Hydroxide Doped Activated Carbon Composites for Phosphate Removal from Synthetic Water: Adsorption and Thermodynamics Studies. *Sustainability* **2022**, *14*, 6991. [[CrossRef](#)]
22. Abushawish, A.; Almanassra, I.W.; Backer, S.N.; Jaber, L.; Khalil, A.K.A.; Abdelkareem, M.A.; Sayed, E.T.; Alawadhi, H.; Shanableh, A.; Atieh, M.A. High-Efficiency Removal of Hexavalent Chromium from Contaminated Water Using Nitrogen-Doped Activated Carbon: Kinetics and Isotherm Study. *Mater. Chem. Phys.* **2022**, *291*, 126758. [[CrossRef](#)]
23. Li, Y.; Wu, Y.; Li, T.; Lu, M.; Chen, Y.; Cui, Y.; Gao, J.; Qian, G. Tuning the Electronic Structure of a Metal–Organic Framework for an Efficient Oxygen Evolution Reaction by Introducing Minor Atomically Dispersed Ruthenium. *Carbon Energy* **2023**, *5*, e265. [[CrossRef](#)]
24. Pan, Y.; Gao, J.; Lv, E.; Li, T.; Xu, H.; Sun, L.; Nairan, A.; Zhang, Q. Integration of Alloy Segregation and Surface Co–O Hybridization in Carbon-Encapsulated CoNiPt Alloy Catalyst for Superior Alkaline Hydrogen Evolution. *Adv. Funct. Mater.* **2023**, *33*, 2303833. [[CrossRef](#)]
25. Zhao, L.; Xu, T.; Lei, X.; Xu, S.; Zhang, F. Scalable Preparation of Alginate Templated-Layered Double Hydroxide Mesoporous Composites with Enhanced Surface Areas and Surface Acidities. *J. Nanosci. Nanotechnol.* **2011**, *11*, 3291–3297. [[CrossRef](#)]
26. Swain, N.; Saravanakumar, B.; Kundu, M.; Schmidt-Mende, L.; Ramadoss, A. Recent Trends in Template Assisted 3D Porous Materials for Electrochemical Supercapacitors. *J. Mater. Chem. A* **2021**, *9*, 25286–25324. [[CrossRef](#)]
27. Li, B.; He, J.; Evans, D.G.; Duan, X. Morphology and Size Control of Ni-Al Layered Double Hydroxides Using Chitosan as Template. *J. Phys. Chem. Solids* **2006**, *67*, 1067–1070. [[CrossRef](#)]
28. Yan, X.; Sahimi, M.; Tsotsis, T.T. Fabrication of High-Surface Area Nanoporous SiOC Ceramics Using Pre-Ceramic Polymer Precursors and a Sacrificial Template: Precursor Effects. *Microporous Mesoporous Mater.* **2017**, *241*, 338–345. [[CrossRef](#)]
29. Coelho, A.; Perrone, O.M.; Gomes, E.; Da-Silva, R.; Thoméo, J.C.; Boscolo, M. Mixed Metal Oxides from Sucrose and Cornstarch Templated Hydrotalcite-like LDHs as Catalysts for Ethyl Biodiesel Synthesis. *Appl. Catal. A Gen.* **2017**, *532*, 32–39. [[CrossRef](#)]
30. Su, H.; Jing, L.; Shi, K.; Yao, C.; Fu, H. Synthesis of Large Surface Area LaFeO<sub>3</sub> Nanoparticles by SBA-16 Template Method as High Active Visible Photocatalysts. *J. Nanoparticle Res.* **2010**, *12*, 967–974. [[CrossRef](#)]
31. Pahalagedara, M.N.; Pahalagedara, L.R.; Kuo, C.H.; Dharmarathna, S.; Suib, S.L. Ordered Mesoporous Mixed Metal Oxides: Remarkable Effect of Pore Size on Catalytic Activity. *Langmuir* **2014**, *30*, 8228–8237. [[CrossRef](#)]
32. Xie, J.; Yamaguchi, T.; Oh, J.-M. Synthesis of a Mesoporous Mg–Al–Mixed Metal Oxide with P123 Template for Effective Removal of Congo Red via Aggregation-Driven Adsorption. *J. Solid State Chem.* **2021**, *293*, 121758. [[CrossRef](#)]
33. An, W.; Ma, J.; Xu, Q. Bio-Template Synthesis of MgAl Layered Double Hydroxide with Enhanced Flame Retardant Property for Leather Finishes. *Appl. Surf. Sci.* **2021**, *551*, 149409. [[CrossRef](#)]
34. Zhao, Y.; Wei, M.; Lu, J.; Wang, Z.L.; Duan, X. Biotemplated Hierarchical Nanostructure of Layered Double Hydroxides with Improved Photocatalysis Performance. *ACS Nano* **2009**, *3*, 4009–4016. [[CrossRef](#)]
35. Sobhana, S.S.L.; Bogati, D.R.; Reza, M.; Gustafsson, J.; Fardim, P. Cellulose Biotemplates for Layered Double Hydroxides Networks. *Microporous Mesoporous Mater.* **2016**, *225*, 66–73. [[CrossRef](#)]
36. Gabal, M.A. Magnetic Properties of NiCuZn Ferrite Nanoparticles Synthesized Using Egg-White. *Mater. Res. Bull.* **2010**, *45*, 589–593. [[CrossRef](#)]
37. Lai, B.H.; Yeh, C.C.; Chen, D.H. Surface Modification of Iron Oxide Nanoparticles with Polyarginine as a Highly Positively Charged Magnetic Nano-Adsorbent for Fast and Effective Recovery of Acid Proteins. *Process Biochem.* **2012**, *47*, 799–805. [[CrossRef](#)]
38. Moshafi, M.H.; Ranjbar, M.; Ilbeigi, G. Biotemplate of Albumen for Synthesized Iron Oxide Quantum Dots Nanoparticles (QDNPs) and Investigation of Antibacterial Effect against Pathogenic Microbial Strains. *Int. J. Nanomed.* **2019**, *14*, 3273–3282. [[CrossRef](#)]
39. Rodríguez-Padrón, D.; Puente-Santiago, A.R.; Luna-Lama, F.; Caballero, Á.; Muñoz-Batista, M.J.; Luque, R. Versatile Protein-Templated TiO<sub>2</sub> Nanocomposite for Energy Storage and Catalytic Applications. *ACS Sustain. Chem. Eng.* **2019**, *7*, 5329–5337. [[CrossRef](#)]
40. Kadam, A.N.; Salunkhe, T.T.; Kim, H.; Lee, S.-W. Biogenic Synthesis of Mesoporous N–S–C Tri-Doped TiO<sub>2</sub> Photocatalyst via Ultrasonic-Assisted Derivatization of Biotemplate from Expired Egg White Protein. *Appl. Surf. Sci.* **2020**, *518*, 146194. [[CrossRef](#)]
41. Maensiri, S.; Masingboon, C.; Laokul, P.; Jareonboon, W.; Promarak, V.; Anderson, P.L.; Seraphin, S. Egg White Synthesis and Photoluminescence of Platelike Clusters of CeO<sub>2</sub> Nanoparticles. *Cryst. Growth Des.* **2007**, *7*, 950–955. [[CrossRef](#)]
42. Stadelman, W.J.; Newkirk, D.; Newby, L. *Egg Science and Technology*; Stadelman, W.J., Cotterill, O.J., Eds.; Avi Publishing: Westport, CT, USA, 1986.
43. Drakos, A.; Kiosseoglou, V. Stability of Acidic Egg White Protein Emulsions Containing Xanthan Gum. *J. Agric. Food Chem.* **2006**, *54*, 10164–10169. [[CrossRef](#)] [[PubMed](#)]
44. Jung, S.Y.; Kim, B.K.; Kim, H.J.; Oh, J.M. Development of Mesopore Structure of Mixed Metal Oxide through Albumin-Templated Coprecipitation and Reconstruction of Layered Double Hydroxide. *Nanomaterials* **2021**, *11*, 620. [[CrossRef](#)]
45. Kooli, F.; Chisem, I.C.; Vucelic, M.; Jones, W. Synthesis and Properties of Terephthalate and Benzoate Intercalates of Mg–Al Layered Double Hydroxides Possessing Varying Layer Charge. *Chem. Mater.* **1996**, *8*, 1969–1977. [[CrossRef](#)]
46. Cullity, B.D.; Stock, S.R. *Elements of X-ray Diffraction*; Prentice Hall: Upper Saddle River, NJ, USA, 2001; p. 388.

47. Yao, W.; Wang, X.; Liang, Y.; Yu, S.; Gu, P.; Sun, Y.; Xu, C.; Chen, J.; Hayat, T.; Alsaedi, A.; et al. Synthesis of Novel Flower-like Layered Double Oxides/Carbon Dots Nanocomposites for U(VI) and <sup>241</sup>Am(III) Efficient Removal: Batch and EXAFS Studies. *Chem. Eng. J.* **2018**, *332*, 775–786. [[CrossRef](#)]
48. Huang, P.P.; Cao, C.Y.; Wei, F.; Sun, Y.B.; Song, W.G. MgAl Layered Double Hydroxides with Chloride and Carbonate Ions as Interlayer Anions for Removal of Arsenic and Fluoride Ions in Water. *RSC Adv.* **2015**, *5*, 10412–10417. [[CrossRef](#)]
49. Birjega, R.; Pavel, O.D.; Costentin, G.; Che, M.; Angelescu, E. Rare-Earth Elements Modified Hydrotalcites and Corresponding Mesoporous Mixed Oxides as Basic Solid Catalysts. *Appl. Catal. A Gen.* **2005**, *288*, 185–193. [[CrossRef](#)]
50. Kim, B.K.; Gwak, G.H.; Okada, T.; Oh, J.M. Effect of Particle Size and Local Disorder on Specific Surface Area of Layered Double Hydroxides upon Calcination-Reconstruction. *J. Solid State Chem.* **2018**, *263*, 60–64. [[CrossRef](#)]
51. Gago, S.; Pillinger, M.; Valente, A.A.; Santos, T.M.; Rocha, J.; Gonçalves, I.S. Immobilization of Oxomolybdenum Species in a Layered Double Hydroxide Pillared by 2,2'-Bipyridine-5,5'-Dicarboxylate Anions. *Inorg. Chem.* **2004**, *43*, 5422–5431. [[CrossRef](#)]
52. Jung, S.-Y.; Kim, B.-K.; Hirata, S.; Inada, M.; Oh, J.-M. Particle Size Effect of Layered Double Hydroxide on the Porosity of Calcined Metal Oxide. *Appl. Clay Sci.* **2020**, *195*, 105701. [[CrossRef](#)]
53. Tanaka, R.; Ogino, I.; Mukai, S.R. Synthesis of Mg-Al Mixed Oxides with Markedly High Surface Areas from Layered Double Hydroxides with Organic Sulfonates. *ACS Omega* **2018**, *3*, 16916–16923. [[CrossRef](#)] [[PubMed](#)]
54. Guo, S.; Jiang, Y.; Li, L.; Huang, X.; Zhuang, Z.; Yu, Y. Thin CuO<sub>x</sub>-Based Nanosheets for Efficient Phenol Removal Benefitting from Structural Memory and Ion Exchange of Layered Double Oxides. *J. Mater. Chem. A* **2018**, *6*, 4167–4178. [[CrossRef](#)]
55. Lin, S.T.; Tran, H.N.; Chao, H.P.; Lee, J.F. Layered Double Hydroxides Intercalated with Sulfur-Containing Organic Solutes for Efficient Removal of Cationic and Oxyanionic Metal Ions. *Appl. Clay Sci.* **2018**, *162*, 443–453. [[CrossRef](#)]
56. Monash, P.; Pugazhenth, G. Utilization of Calcined Ni-Al Layered Double Hydroxide (LDH) as an Adsorbent for Removal of Methyl Orange Dye from Aqueous Solution. *Environ. Prog. Sustain. Energy* **2014**, *33*, 154–159. [[CrossRef](#)]
57. Kim, B.K.; Lee, D.Y.; Gwak, G.H.; Han, Y.S.; Oh, J.M. Zn-Fe Mixed Metal Oxides from Metal Hydroxide Precursor: Effect of Calcination Temperature on Phase Evolution, Porosity, and Catalytic Acidity. *J. Solid State Chem.* **2019**, *269*, 454–458. [[CrossRef](#)]
58. Li, J.; Zhang, N.; Ng, D.H.L. Synthesis of a 3D Hierarchical Structure of  $\gamma$ -AlO(OH)/Mg-Al-LDH/C and Its Performance in Organic Dyes and Antibiotics Adsorption. *J. Mater. Chem. A* **2015**, *3*, 21106–21115. [[CrossRef](#)]
59. Gonzalez Rodriguez, P.; de Ruiter, M.; Wijnands, T.; ten Elshof, J.E. Porous Layered Double Hydroxides Synthesized Using Oxygen Generated by Decomposition of Hydrogen Peroxide. *Sci. Rep.* **2017**, *7*, 481. [[CrossRef](#)]
60. Aramendía, M.A.; Avilés, Y.; Borau, V.; Luque, J.M.; Marinas, J.M.; Ruiz, J.R.; Urbano, F.J. Thermal Decomposition of Mg/Al and Mg/Ga Layered-Double Hydroxides: A Spectroscopic Study. *J. Mater. Chem.* **1999**, *9*, 1603–1607. [[CrossRef](#)]
61. Karuppasamy, K.; Vikraman, D.; Bose, R.; Hussain, S.; Santhoshkumar, P.; Manikandan, R.; Jung, J.; Alameri, S.; Alfantazi, A.; Kim, H.-S. Unveiling the Redox Electrochemical Kinetics of Interconnected Wrinkled Microspheres of Binary Cu<sub>2-x</sub>Se/Ni<sub>1-x</sub>Se as Battery-Type Electrode for Advanced Supercapacitors. *J. Colloid Interface Sci.* **2024**, *654*, 1098–1110. [[CrossRef](#)]

**Disclaimer/Publisher's Note:** The statements, opinions and data contained in all publications are solely those of the individual author(s) and contributor(s) and not of MDPI and/or the editor(s). MDPI and/or the editor(s) disclaim responsibility for any injury to people or property resulting from any ideas, methods, instructions or products referred to in the content.